Electronic Supplementary Material (ESI) for ChemComm.

Supplementary Information

Structural-Failure Resistance of Metal-Organic Frameworks toward Multiple-Cycle CO_2 Sorption

Zhigang Hu,[a, †] Yao Sun,[b, †] Kaiyang Zeng,[b, *] and Dan Zhao[a, *]

[a] Department of Chemical and Biomolecular Engineering, National University of Singapore, 4 Engineering Drive 4, 117585 Singapore
[b] Department of Mechanical Engineering, National University of Singapore, 9 Engineering Drive 1, 117576 Singapore

[†] These authors contribute equally to this work.

Correspondence and requests for materials should be addressed to D.Z. (E-mail: chezhao@nus.edu.sg) or K.Z. (mpezk@nus.edu.sg).

Materials and Methods

All the reagents were obtained from commercial suppliers and used without further purification. Field-emission scanning electron microscope (FE-SEM) analyses were conducted on an FEI Quanta 600 SEM (20 kV) equipped with an energy dispersive spectrometer (EDS, Oxford Instruments, 80 mm^2 detector). Samples were treated via Pt sputtering before observation. Powder X-ray diffraction patterns were obtained on a Bruker D8 Advance X-ray powder diffractometer equipped with a Cu sealed tube ($\lambda = 1.54178$ Å) at a scan rate of 0.02 deg s^{-1}. Thermogravimetric analyses (TGA) were performed using a Shimadzu DTG-60AH thermal analyzer under flowing N_2 with a heating rate of 10 °C min^{-1}.

Low-Pressure Gas Sorption Measurements

Gas sorption isotherms were measured up to 1 bar using a Micromeritics ASAP 2020 surface area and pore size analyzer. Before the measurements, the samples (~50 mg) were degassed under reduced pressure ($< 10^{-2}$ Pa) at 150 °C for 12 h. UHP grade N_2, He, and CO_2 were used for all the measurements. Oil-free vacuum pumps and oil-free pressure regulators were used to prevent contamination of the samples during the degassing process and isotherm measurement. Pore size distribution data were calculated from the N_2 sorption isotherms at 77 K based on non-local density functional theory (NLDFT) model (assuming slit pore geometry) and Barrett-Joyner-Halenda (BJH) desorption model in the Micromeritics ASAP 2020 software package.

Solvothermal Synthesis of MOFs

HKUST-1 was synthesized based on the reported procedure.[1] UiO-66 was synthesized as follows.[2] Briefly, benzene-1,4-dicarboxylic acid (BDC) (166 mg) and $ZrCl_4$ (240 mg) dissolved in 18 mL of DEF/formic acid (16/2, v/v) mixed solvent were loaded into a Teflon lined autoclave and heated at 123 °C for 24 hours. The product was soaked in anhydrous methanol for 3 days at room temperature, during which time the extract was decanted and fresh methanol was added every day. Then the sample was treated with anhydrous dichloromethane similarly for another 3 days. This process was carried out to wash out residual reagents in the pores. After removal of dichloromethane by decanting, the sample was dried under a dynamic vacuum at 120 °C for 24 h to yield the final product with a yield of 75% based on the overall weight of ligand and metal salt.

Sample Preparation for MAFM Study

In a typical sample preparation process, dry MOF powder (~10 mg) was evenly dispersed into ethanol, which was further pipetted onto a clean silicon wafer substrate. The silicon wafer substrate was then left dry at 80°C for 2 h in the presence of inert gas. During our measurement, the contact stiffness mapping containing 256×256 test points was obtained synchronously with *in-situ* topography mapping. For all the experiments, a silicon probe (AC160TS, Olympus, Japan) with a spring constant of 42 N m^{-1} was applied. The indent elastic modulus mapping was transformed from the corresponding calculations.

Principle of MAFM Study[3]

The multifrequency AFM under AM-FM mode refers to a simultaneous excitation of two modes of the probe cantilever. Through simultaneous excitation of two bending vibration modes of the cantilever, fast imaging of both morphology and elastic property of nanomaterials can be achieved.[4] The excitation frequency is typically selected at a resonant frequency of each mode while actuating multiple intrinsic modes improves the coupling between different modes. Since the probe cantilever has different resonant frequencies, elastic constants and quality factors, different modal vibrations can thus provide different properties with different sensitivities.[3a] Multifrequency (Bimodal) AFM uses the first modal amplitude or frequency as a feedback on the sample surface topography imaging, while second modal amplitude, phase and frequency shifts can be changed freely without a feedback loop, which can be used to analyse the mechanical and electromagnetical properties.[3a]

In this technique, the relationship of force gradient between tip and sample and second modal frequency can be expressed as

$$k_{ts} \approx 2k_2 \Delta f_2 / f_2^0 \qquad [1]$$

Where k_{ts}, k_2, f_2^0, and Δf_2 are the force gradient between tip and sample, second mode elastic constant of the probe, second mode free vibration resonance frequency of the probe and tip-sample second mode contact resonance frequency shift, respectively. Assuming that the tip-sample contact is Herz contact,[5] the relationship between the force gradient between tip and sample and tip-sample equivalent elastic modulus can be written as

$$k_{ts} = 2a_c E^* \qquad [2]$$

Herein, α_c is the contact radius between tip and the sample, and E^* is the tip-sample equivalent elastic modulus. According to the equations [1] and [2] above, E^* is a linear function of Δf_2, with a constant coefficient C.

$$E^* = k_2 \Delta f_2 / a_c f_2^0 = C\Delta f_2 \tag{3}$$

Because of the uncertainty of contact radius, a reference material with a known elastic modulus is usually used to calibrate and calculate the elastic modulus of the sample. If the elastic modulus of the reference material is similar to that of the sample, the contact radius of tip-reference material is postulated to be same with tip-sample contact radius. The constant coefficient C could be determined by replicating the same experiment and obtaining a relationship between equivalent elastic modulus and second mode contact resonance frequency shift on the reference material.

For Herz contact model, the contact stiffness between tip and sample is a first derivative of applied pressure to deformation which can be written as

$$k^* = \frac{\delta F_N}{\delta\delta} = \sqrt[3]{6E^{*2}RF_N} \tag{4}$$

δ, F_N and R are the deformation, applied force and tip radius, respectively. If a single reference material is adopted, the relationship between contact stiffness and equivalent elastic modulus can be obtained:

$$E^*_{s-tip} = E^*_{ref-tip}\left(\frac{k^*_{s-tip}/k_c}{k^*_{ref-tip}/k_c}\right)^n \tag{5}$$

Where $E^*_{s\text{-}tip}$, $E^*_{ref\text{-}tip}$, $k^*_{s\text{-}tip}$, $k^*_{ref\text{-}tip}$, and k_c are tip-sample equivalent elastic modulus, tip-reference material equivalent elastic modulus, tip-sample contact stiffness, tip-reference material contact stiffness and cantilever spring constant, respectively. As for Herz contact model, E^* can be written as

$$E^* = \frac{1}{M_t} + \frac{1}{M_s} \qquad [6]$$

M_t and M_s are indentation elastic modulus of the tip and sample, respectively.

Calculations of Isosteric Heat of Adsorption (Q_{st})[6]

The CO_2 and N_2 adsorption isotherms measured at 273 K and 298 K were first fitted to a virial equation (Equation 7). The fitting parameters were then used to calculate the isosteric heat of adsorption (Q_{st}) using Equation 8,

$$\ln P = \ln N + \frac{1}{T}\sum_{i=0}^{m} a_i N^i + \sum_{i=0}^{n} b_i N^i \qquad [7]$$

$$Q_{st} = -R\sum_{i=0}^{m} a_i N^i \qquad [8]$$

where P is pressure (mmHg), N is adsorbed quantity (mmol g^{-1}), T is temperature (K), R is gas constant (8.314 J K^{-1} mol^{-1}), a_i and b_i are virial coefficients, m and n represent the number of coefficients required to adequately describe the isotherms (herein, $m = 5$, $n = 2$).

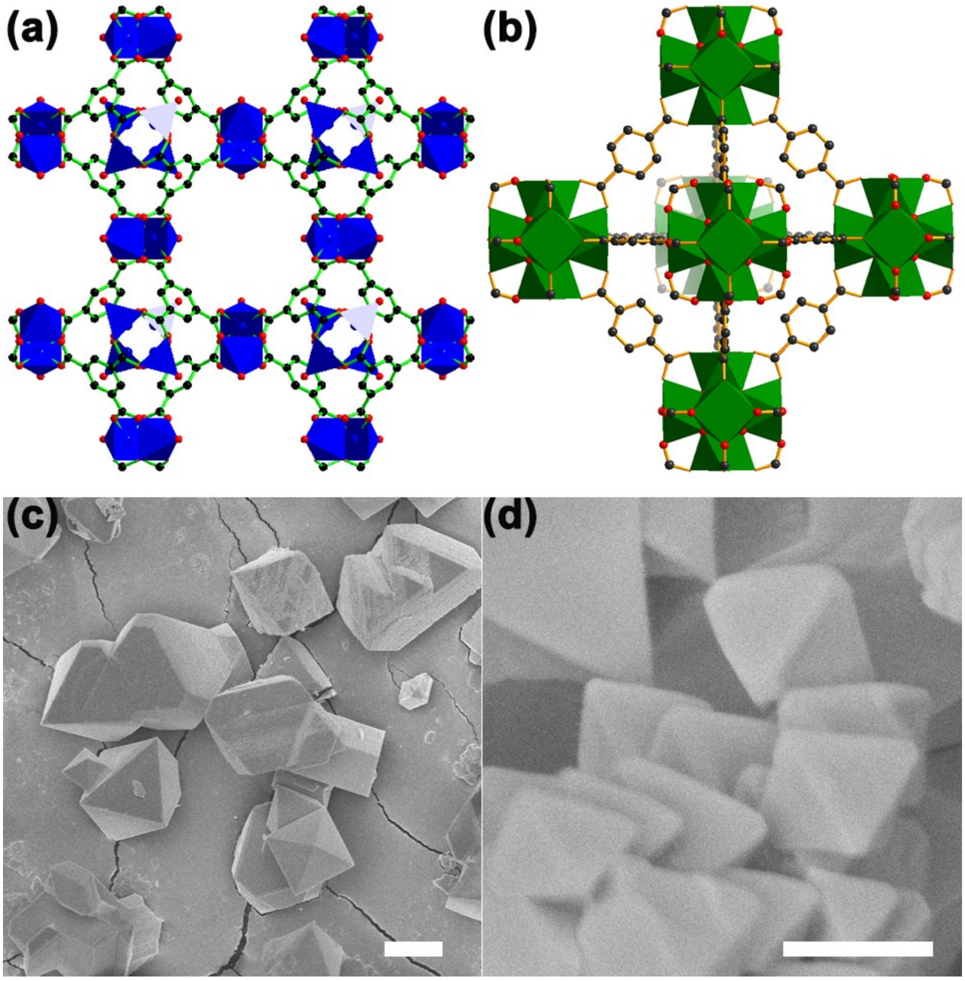

Figure S1. Crystal structure of HKUST-1 (a) and UiO-66(Zr) (b); FE-SEM images of HKUST-1 (c) and UiO-66(Zr) (d). Scale bar: 500 nm.

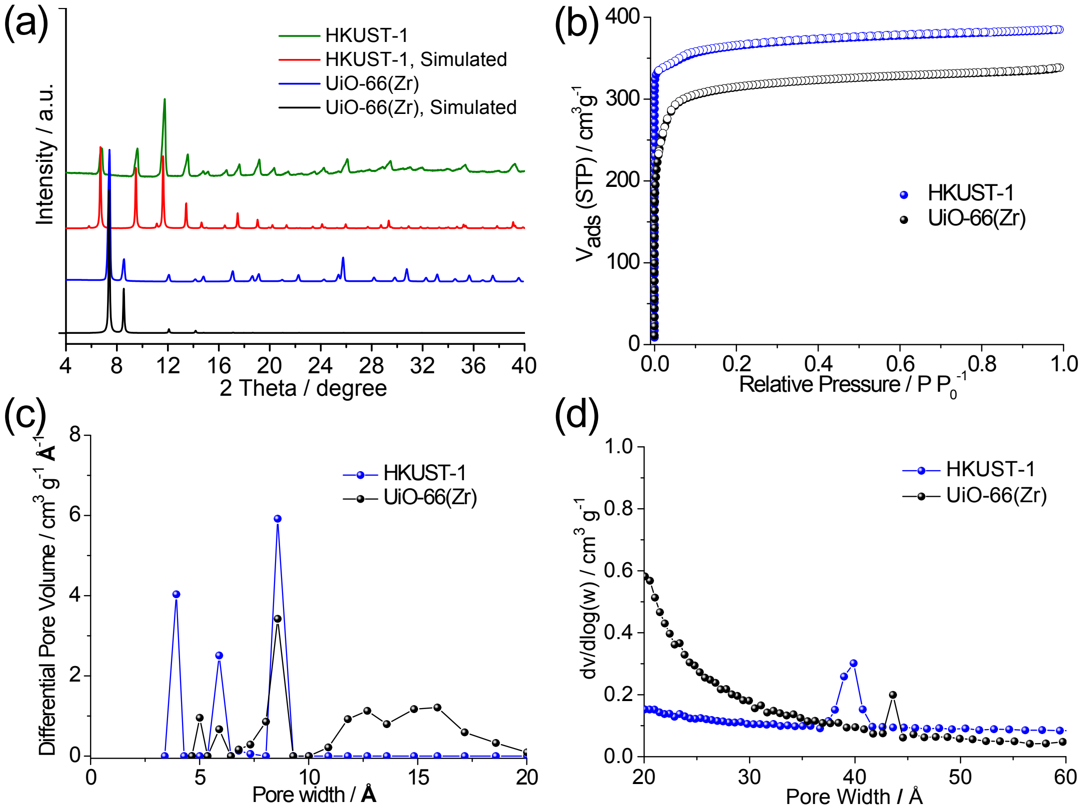

Figure S2. Structural and porosity characterizations of HKUST-1 and UiO-66(Zr): (a) powder X-ray diffraction (PXRD) patterns; (b) N_2 sorption isotherms at 77 K; (c) pore size distribution calculated from non-local density functional theory (NLDFT) model (assuming slit pore geometry); (d) pore size distribution calculated from Barrett-Joyner-Halenda (BJH) desorption model.

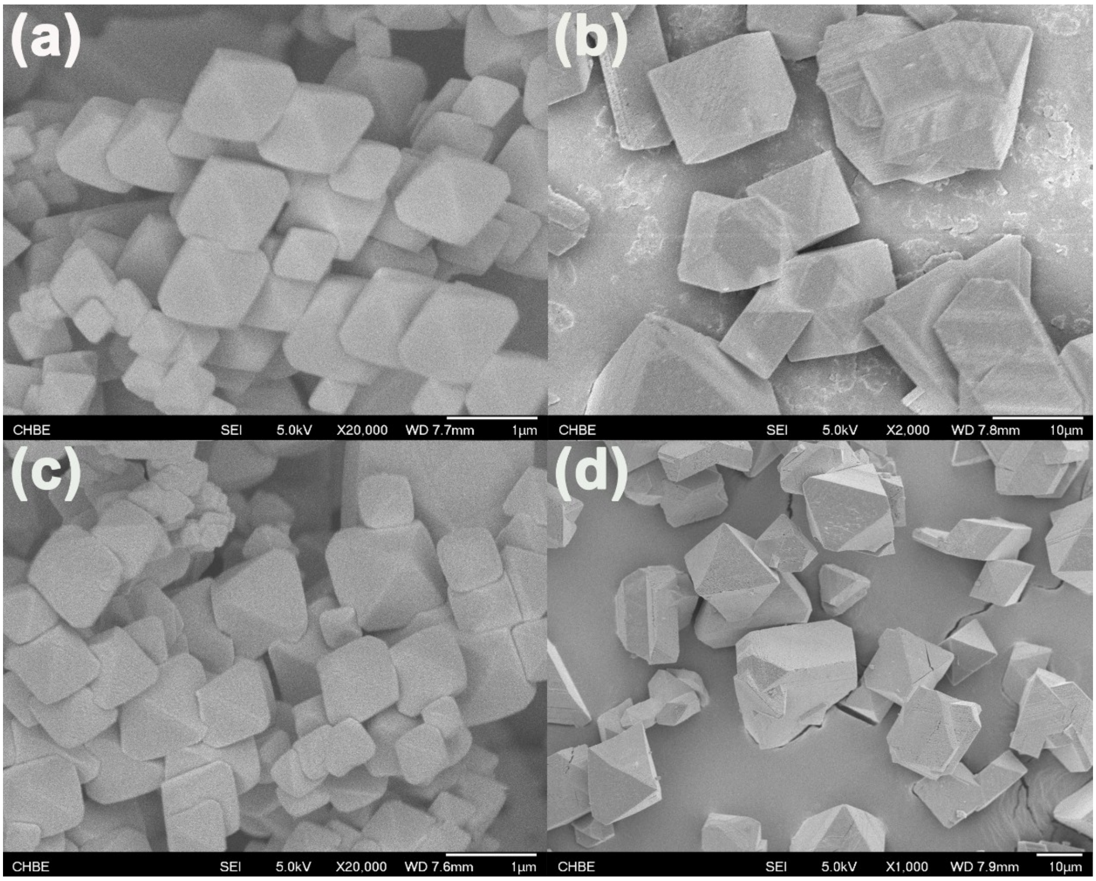

Figure S3. FE-SEM images of UiO-66(Zr) (a, c) and HKUST-1 (b, d) before (a-b) and after (c-d) multiple-cycle CO_2 adsorption-desorption tests.

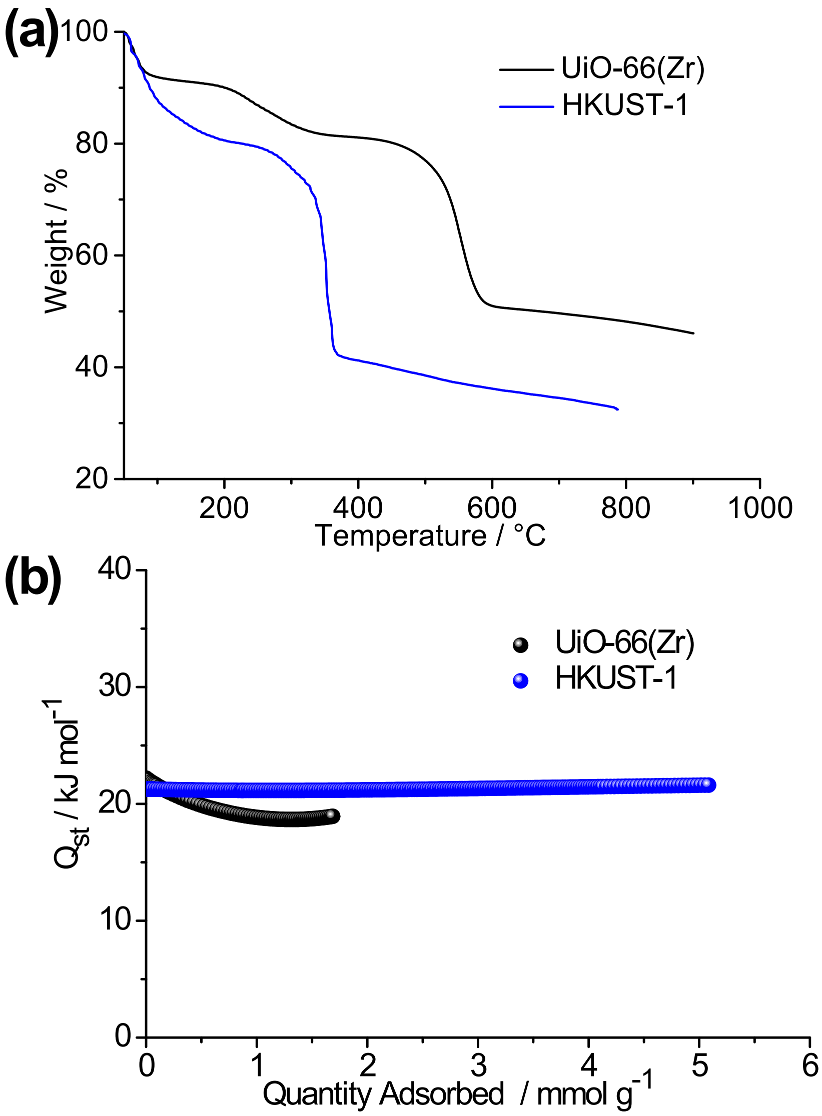

Figure S4. Thermogravimetric analysis (TGA) curves (a) and isosteric heat of CO_2 adsorption values (b) for UiO-66(Zr) and HKUST-1.

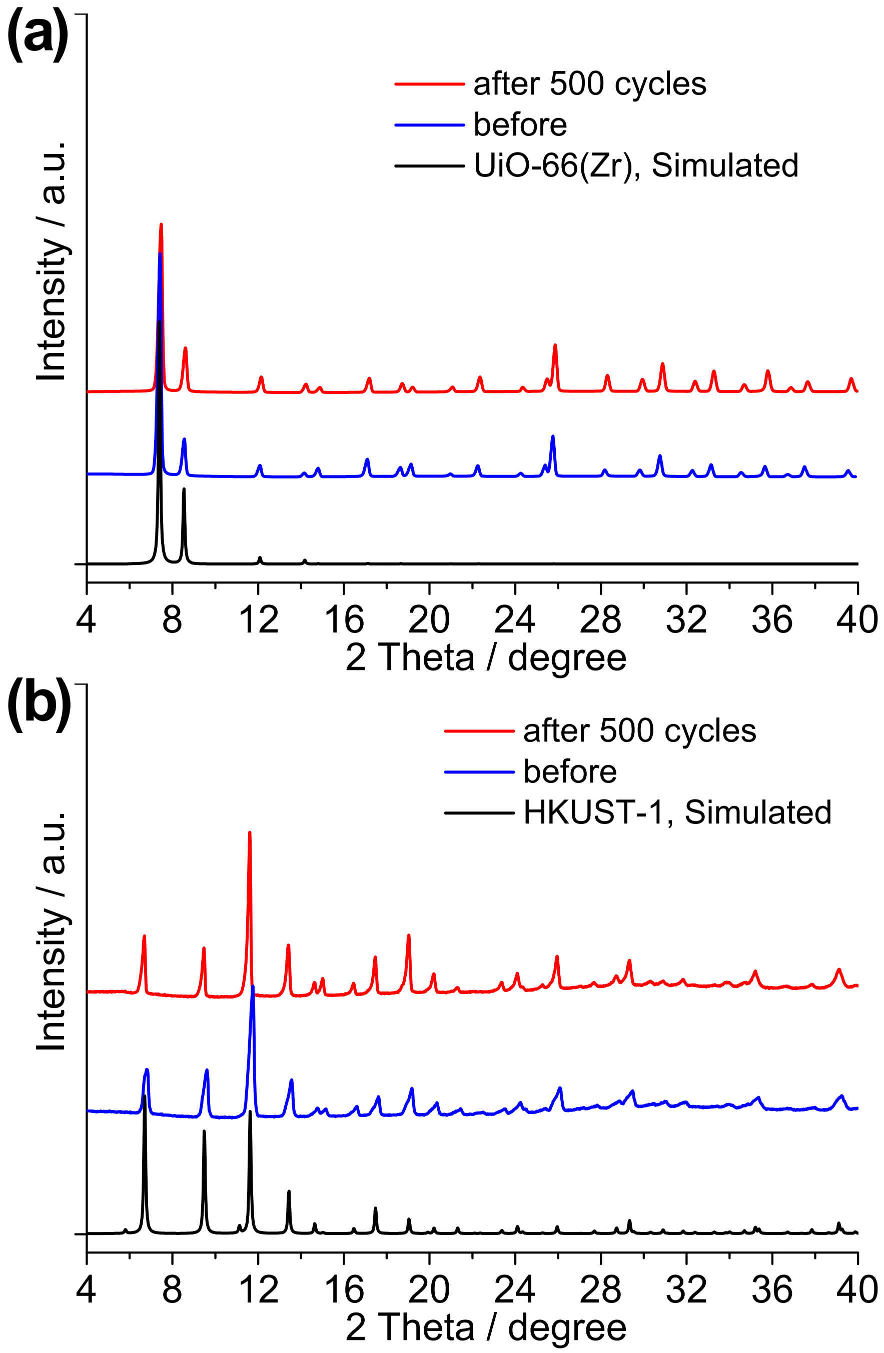

Figure S5. PXRD patterns of UiO-66(Zr) (a) and HKUST-1 (b) before and after 500-cycle CO_2 adsorption-desorption experiments.

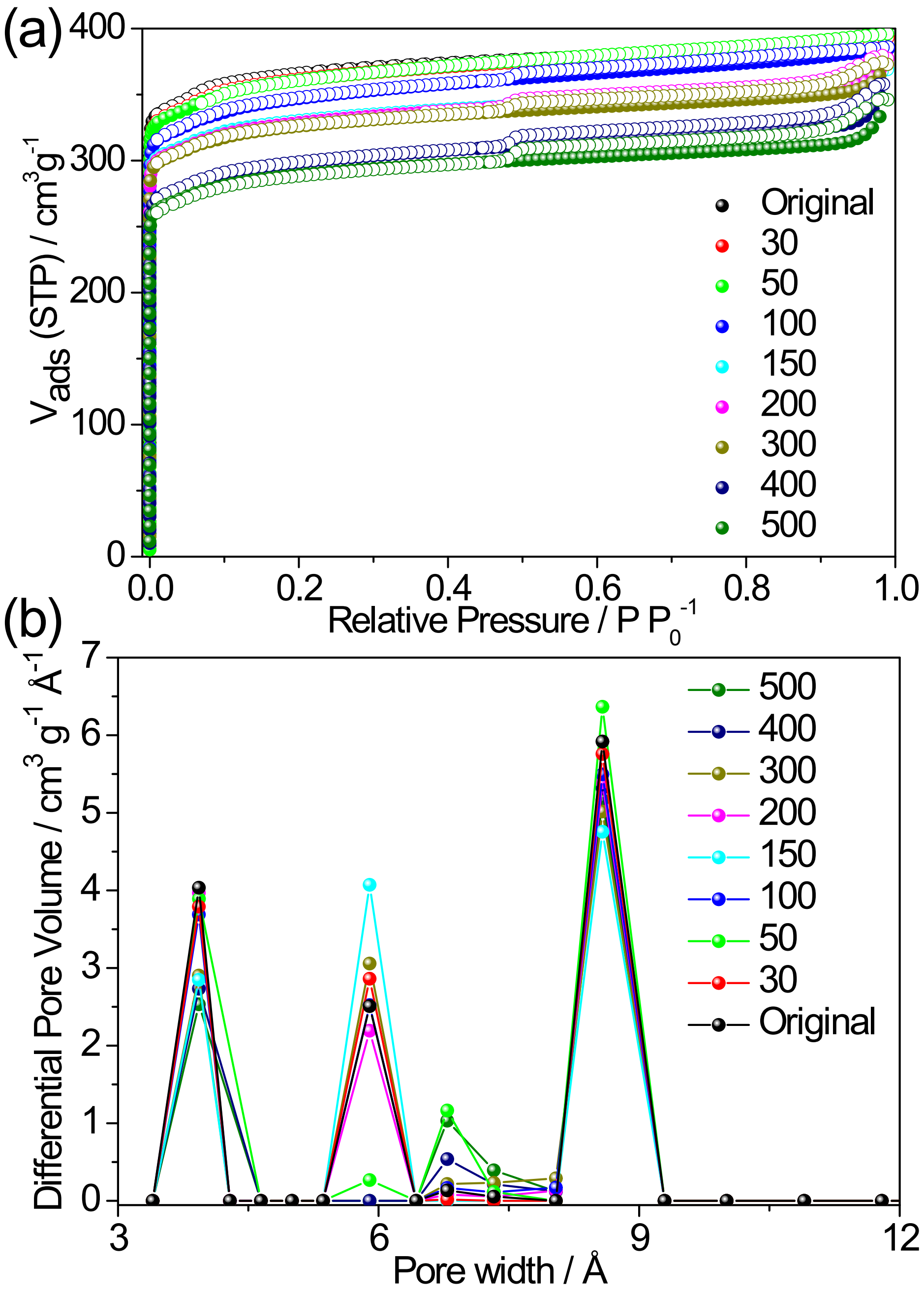

Figure S6. 77 K N_2 sorption isotherms (a) and non-local density functional theory (NLDFT) pore size distribution (b) of HKUST-1 after different CO_2 adsorption-desorption cycles.

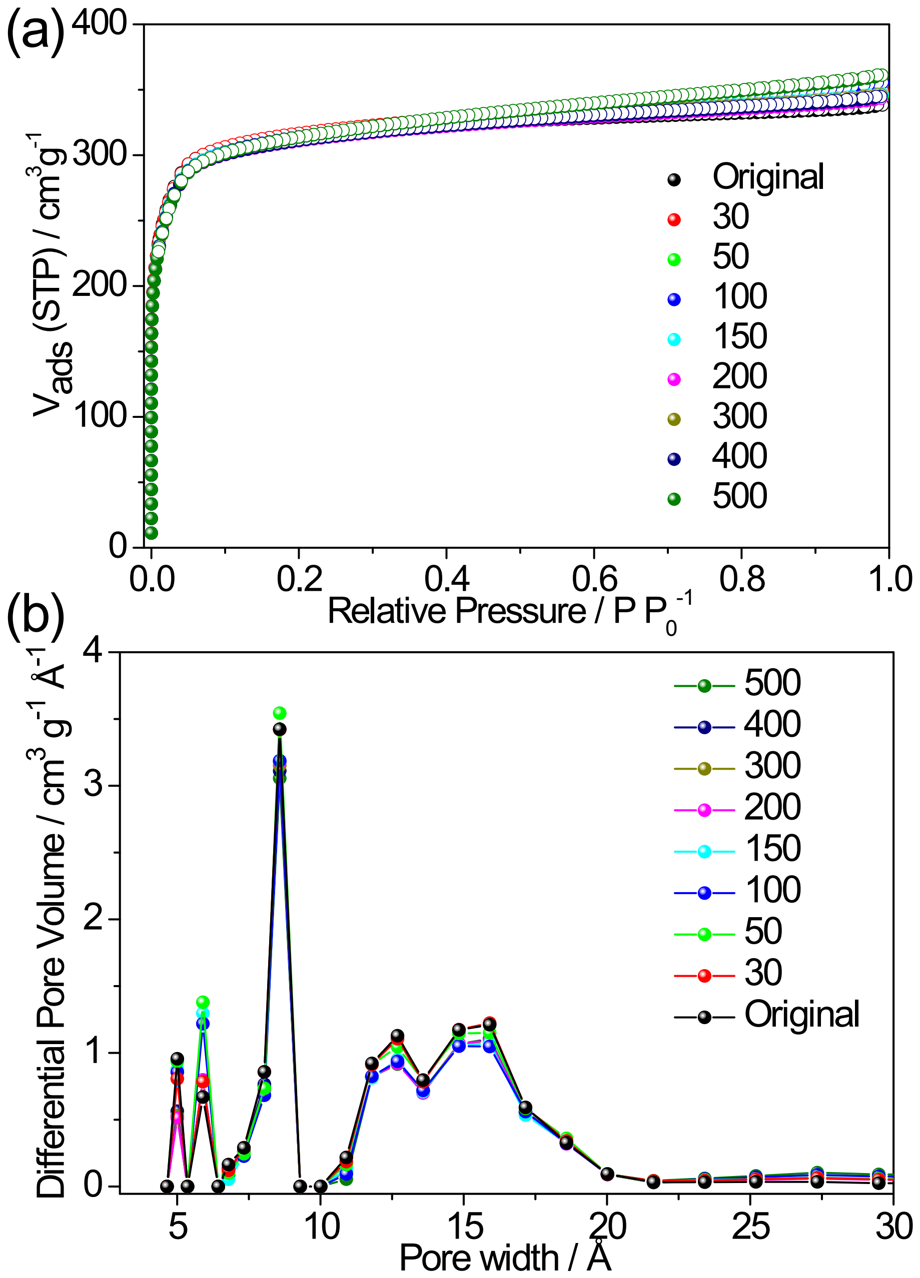

Figure S7. 77 K N_2 sorption isotherms (a) and non-local density functional theory (NLDFT) pore size distribution (b) of UiO-66(Zr) after different CO_2 adsorption-desorption cycles.

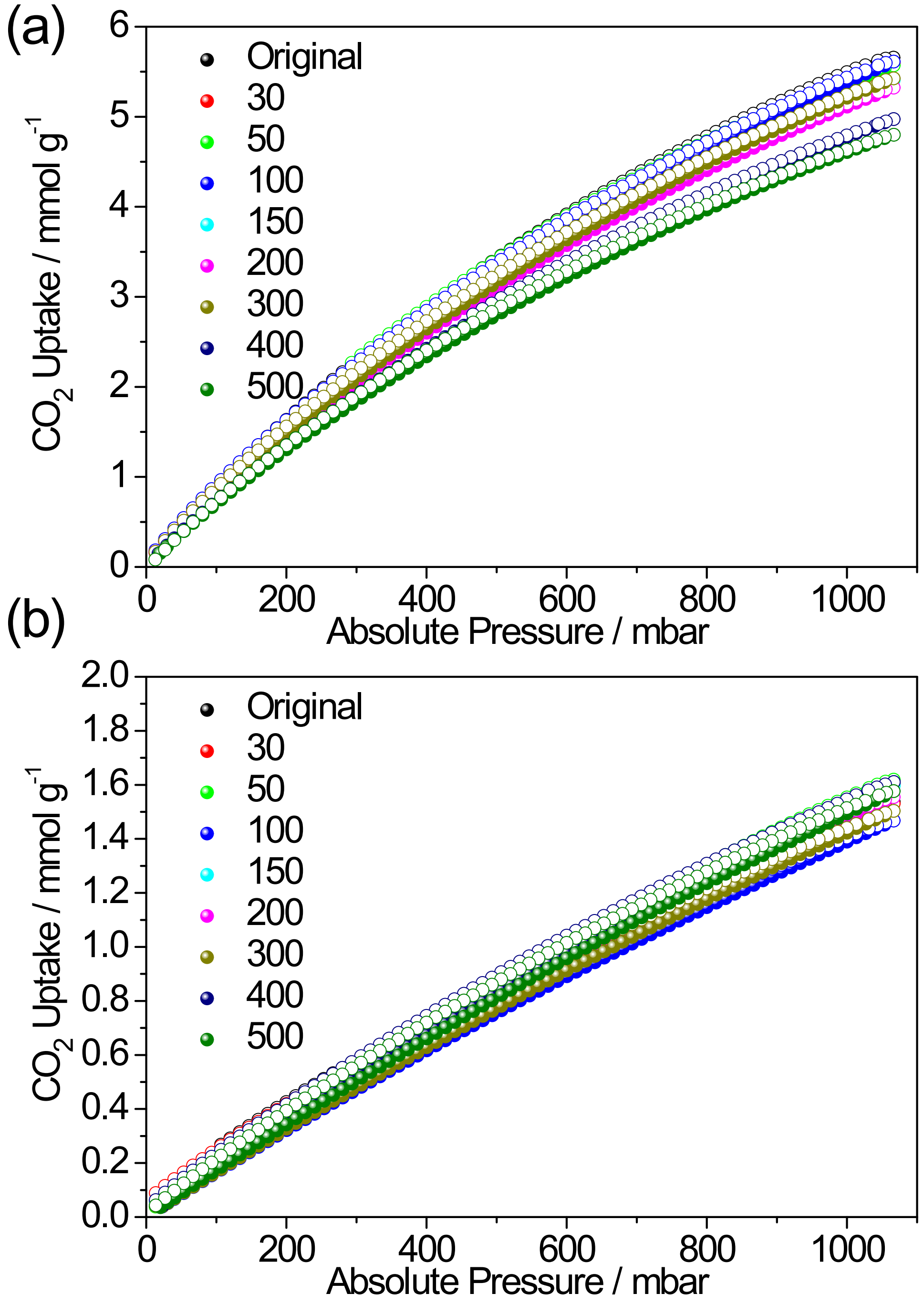

Figure S8. CO$_2$ sorption isotherms at 298 K of HKUST-1 (a) and UiO-66(Zr) (b) after different CO$_2$ adsorption-desorption cycles.

Table S1. Multiple-cycle CO_2 adsorption-desorption test results of UiO-66(Zr) and HKUST-1.

Cycle Number	**UiO-66(Zr)**			**HKUST-1**		
	BET S.A.[a)]	Pore Volume[b)]	CO_2 uptake[c)]	BET S.A.[a)]	Pore Volume[b)]	CO_2 uptake[c)]
0	1180	0.52	1.52	1670	0.729	5.41
30	1190	0.54	1.51	1663	0.726	5.37
50	1176	0.53	1.53	1668	0.731	5.35
80	N.A.	N.A.	N.A.	1665	0.729	5.39
100	1195	0.55	1.49	1665	0.733	5.37
150	1182	0.53	1.51	1565	0.703	5.19
170	N.A.	N.A.	N.A.	1562	0.716	5.21
200	1179	0.53	1.49	1553	0.699	5.11
250	1185	0.53	1.51	1540	0.699	5.09
300	1180	0.53	1.52	1536	0.691	5.21
320	N.A.	N.A.	N.A.	1530	0.687	5.17
360	N.A.	N.A.	N.A.	1512	0.726	5.04
400	1185	0.53	1.52	1392	0.661	4.77
500	1190	0.55	1.49	1270	0.614	4.61

[a)] $m^2\ g^{-1}$; [b)] $cm^3\ g^{-1}$; [c)] $mmol\ g^{-1}$; N.A. not applicable.

References

1 J. L. C. Rowsell and O. M. Yaghi, *J. Am. Chem. Soc.*, 2006, **128**, 1304.

2 Z. Hu, K. Zhang, M. Zhang, Z. Guo, J. Jiang and D. Zhao, *ChemSusChem*, 2014, **7**, 2791.

3 (a) R. Garcia and E. T. Herruzo, *Nat. Nanotechnol.*, 2012, **7**, 217; (b) T. Li and K. Zeng, *Nanoscale*, 2014, **6**, 2177; (c) A. K. Chaudhari, I. Han and J.-C. Tan, *Adv. Mater.*, 2015, **27**, 4438.

4 G. Chawla and S. D. Solares, *Appl. Phys. Lett.*, 2011, **99**, 074103.

5 R. Garcia and R. Proksch, *Eur. Polym. J.*, 2013, **49**, 1897.

6 J. L. C. Rowsell and O. M. Yaghi, *J. Am. Chem. Soc.*, 2006, **128**, 1304.